Supporting Information

Unveiling Reaction Dynamics and Degradation Pathways in Microwave-Synthesized Antimony Anodes for Na-Ion Batteries

*Daniel Schuhmacher[a], Fabio Maroni[a], Jonathan Delaney[a], Ali Ahmadian[b,c], Mario Marinaro[a,]**

[a]ZSW-Zentrum für Sonnenenergie und Wasserstoff-Forschung,

Helmholtzstrasse 8, 89081, Ulm, Germany

[b]Helmholtz Institute Ulm for Electrochemical Energy Storage (HIU), Karlsruhe Institute of Technology,

Helmholtzstrasse 11, 89081, Ulm, Germany

[c]Karlsruhe Nano Micro Facility (KNMFi), Karlsruhe Institute of Technology (KIT),

Kaiserstraße 12, 76131 Karlsruhe, Germany

*Corresponding author: mario.marinaro@zsw-bw.de

FIGURES AND TABLES

Table S1. Parameters obtained from Rietveld Refinement of Sb–C using reducing agent NaH_2PO_2.

Space group atom	$R\bar{3}m$ site	x	y	z	Occ.
Sb	6	0	0	0.23385	1

a = 4.308 Å / c = 11.278 Å / V = 181.307 Å^3 / LVol-IB = 90 nm / LVol-FWHM = 126 nm / R_{exp} = 2.97 / R_p = 7.44 / R_{wp} = 10.18 / χ^2 = 3.4

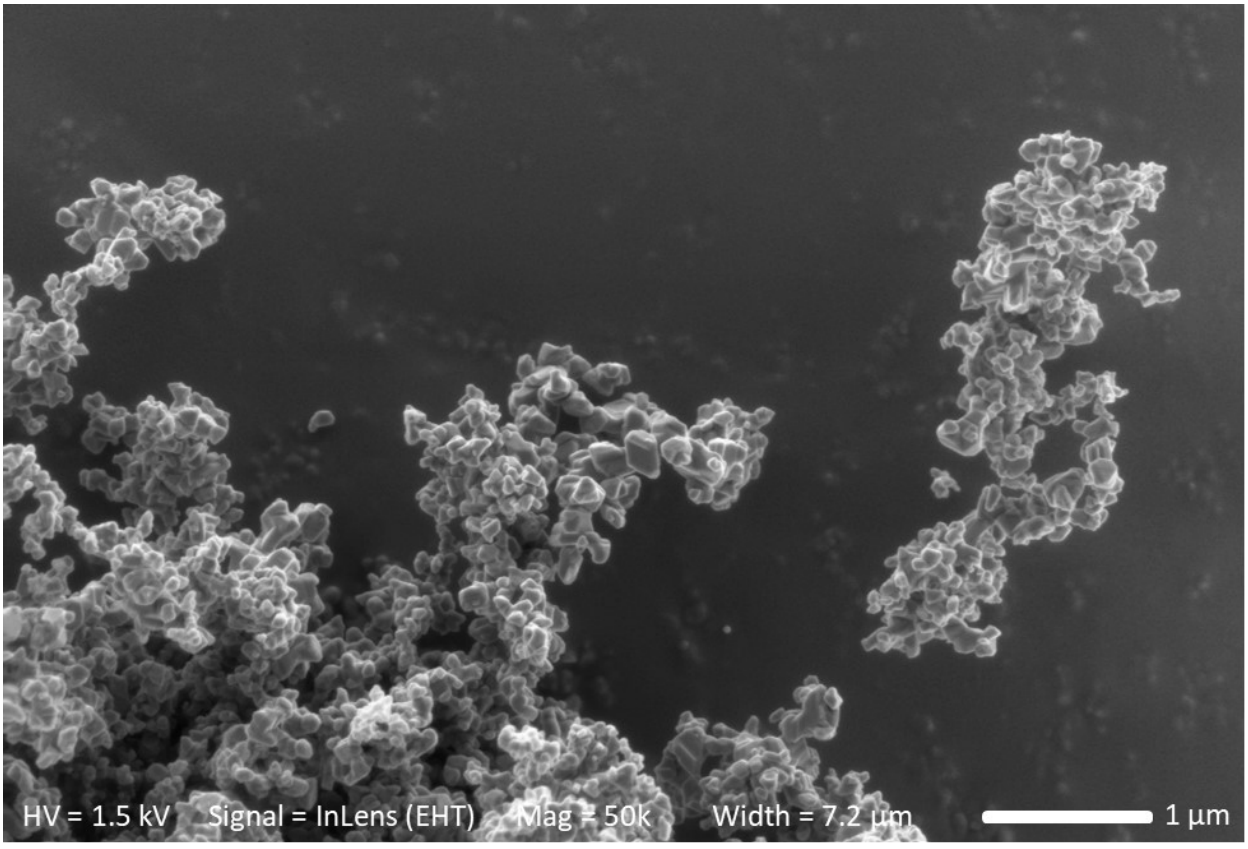

Figure S1. SEM image of Sb-C at 50 kX magnification.

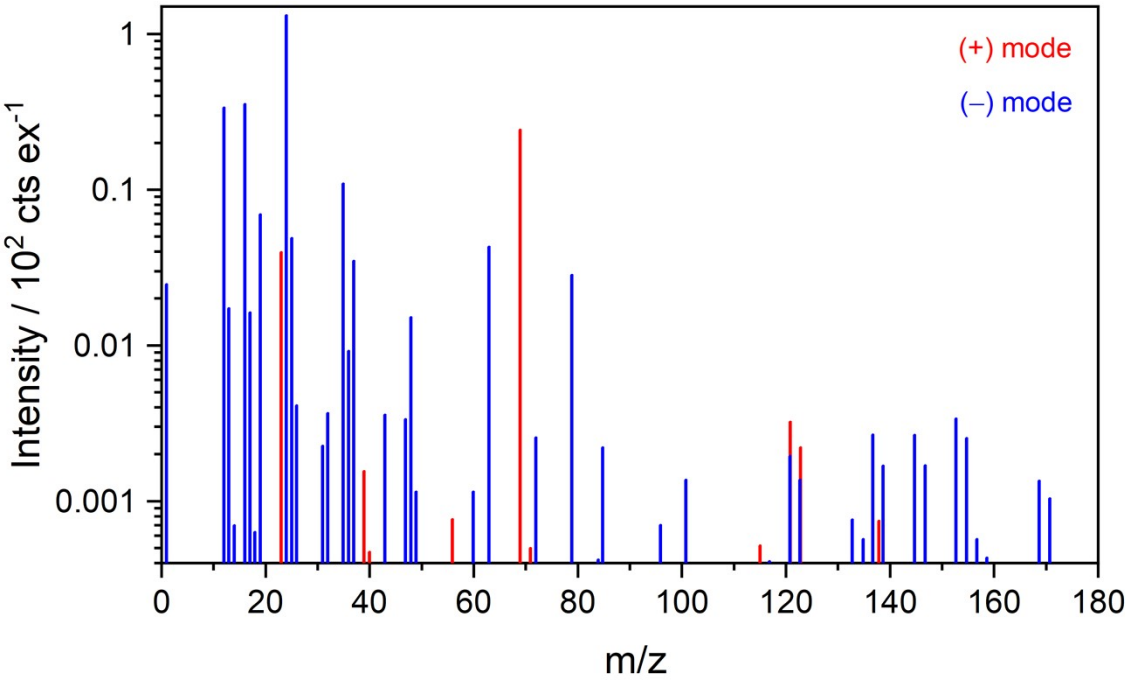

Figure S2. TOF-SIMS spectra obtained from a Sb-C agglomerate with y-axis plotted in logarithmic scale to highlight minor intensities.

Table S2. Probable (and possible) fragments identified by TOF-SIMS analysis.[1–9]

m/z	fragment (+)	m/z	fragment (-)	m/z	fragment (-)	m/z	fragment (-)
12	C^+	1	H^-	32	S^-/O_2 (PH^-)	85	GaO^-
23	Na^+	12	C^-	35/37	Cl^-	96	C_8^-
24	C_2^+	13	CH^-	36	C_3^-	101	GaO_2^-
31	P^+	14	CH_2^- (N^-)	43	(CP^-)	117	GaO_3^-
39	K^+	16	O^-	47	PO^-	121/123	Sb^-
40	Ca^+	17	OH^-	48	C_4^-	133/135	SbC^-
56	Fe^+	18	H_2O^-	49	C_4H^-	137/139	SbO^-
69/71	Ga^+	19	F^-	60	C_5^-	145/147	SbC_2^-
115	In^+	24	C_2^-	63	PO_2^-	153/155	SbO_2^-
121/123	Sb^+	25	C_2H^-	72	C_6^-	157/159	SbC_3^-
138	Ba^+	26	(CN^-)	79	PO_3^- (Br^-)	171/169	SbO_3^- / SbC_4^-
		31	P^-	84	C_7^-		

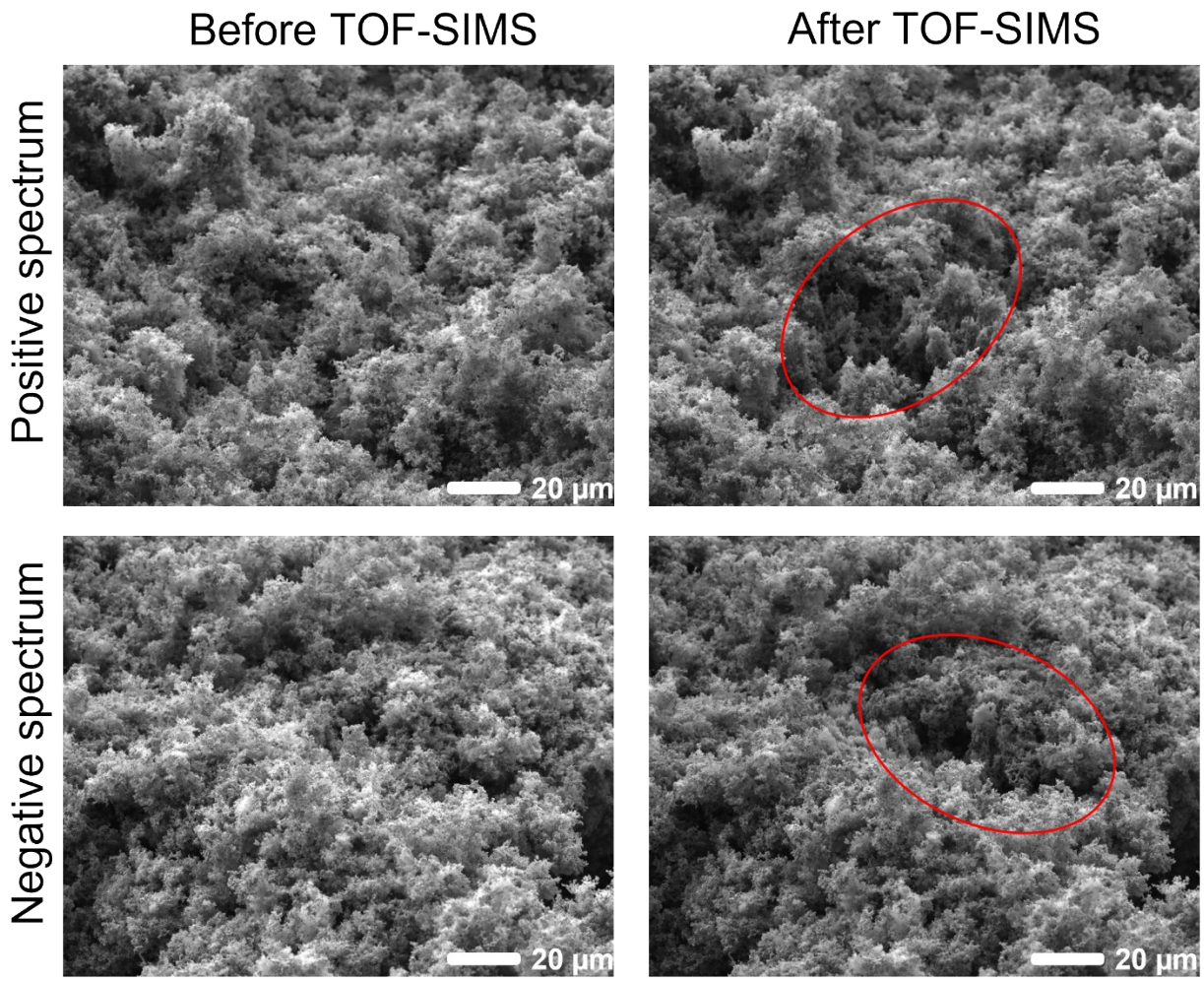

Figure S3. The FIB-SEM image of the surface of a Sb–C agglomerate showing the area selected for TOF-SIMS analysis before and after Ga^+ bombardment (red circle). Signal: secondary electrons; accelerating voltage: 5 keV.

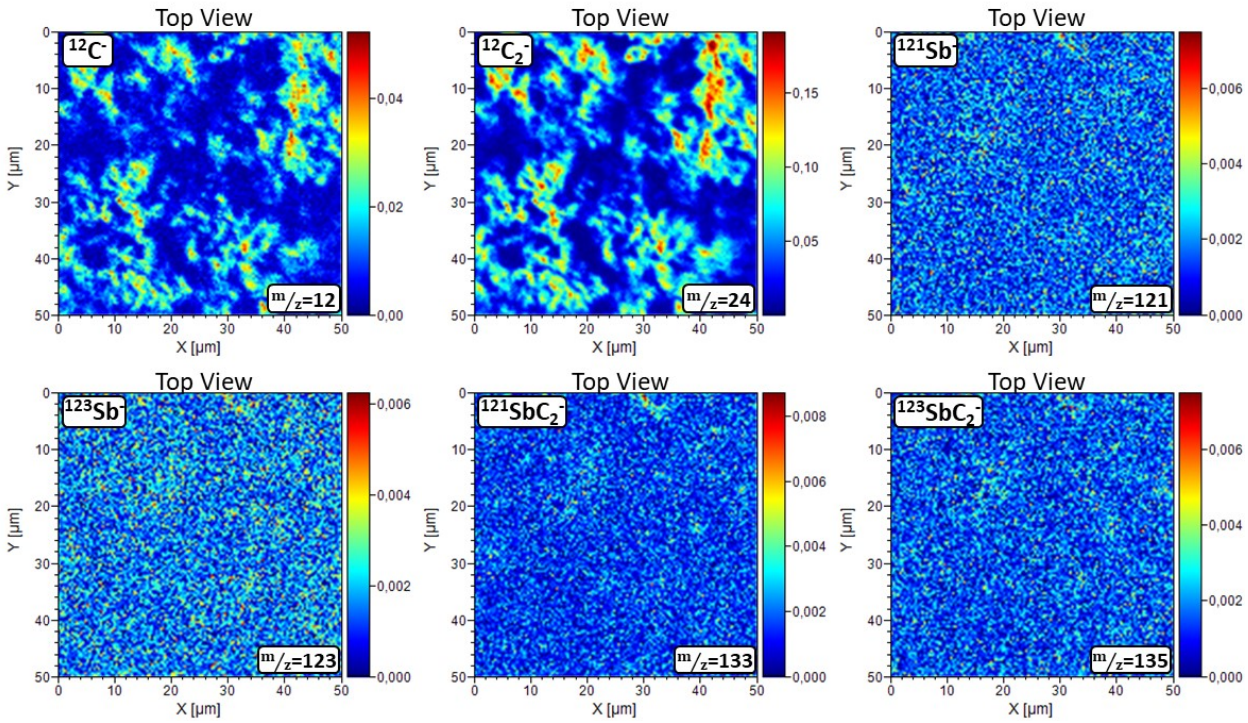

Figure S4. Lateral profiles of Sb and C species in the field of view of the TOF-SIMS. Topography can affect the TOF-SIMS profile of the fragments.[10] Thus, the profiles of the high intensity fragments C^- and C_2^- can reflect topographical differences in the field of view of the TOF-SIMS (see Figure S3), which is helpful in interpreting the other profiles.

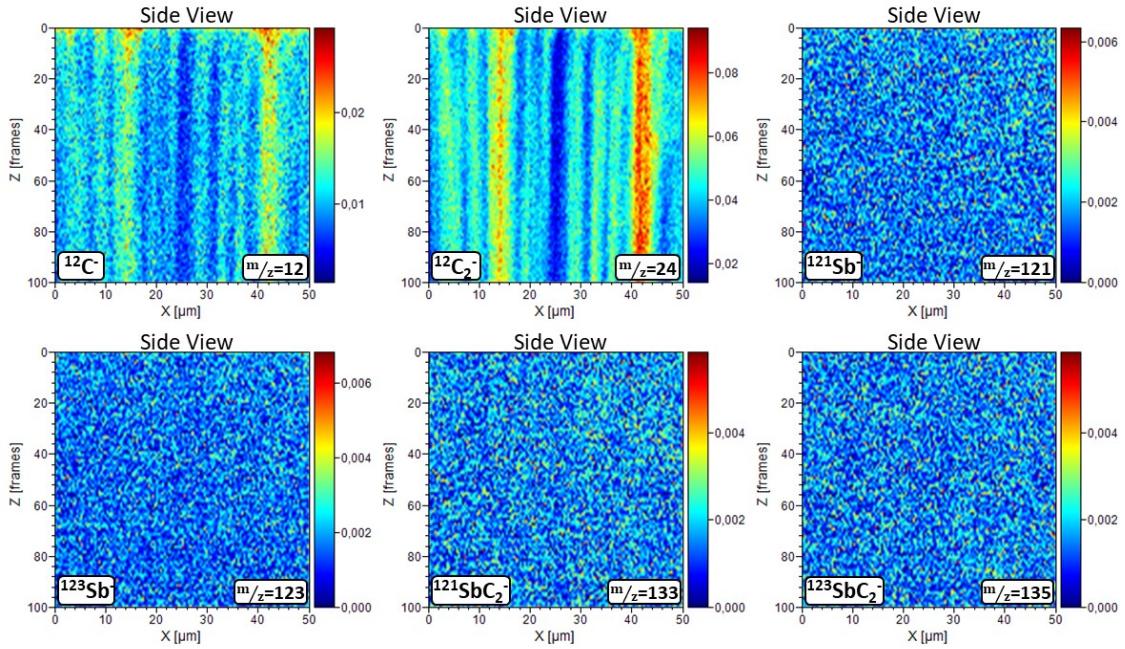

Figure S5. Side profiles of Sb and C species in the field of view of the TOF-SIMS. The profiles of the high intensity fragments C^- and C_2^- can include a contribution from the topography.

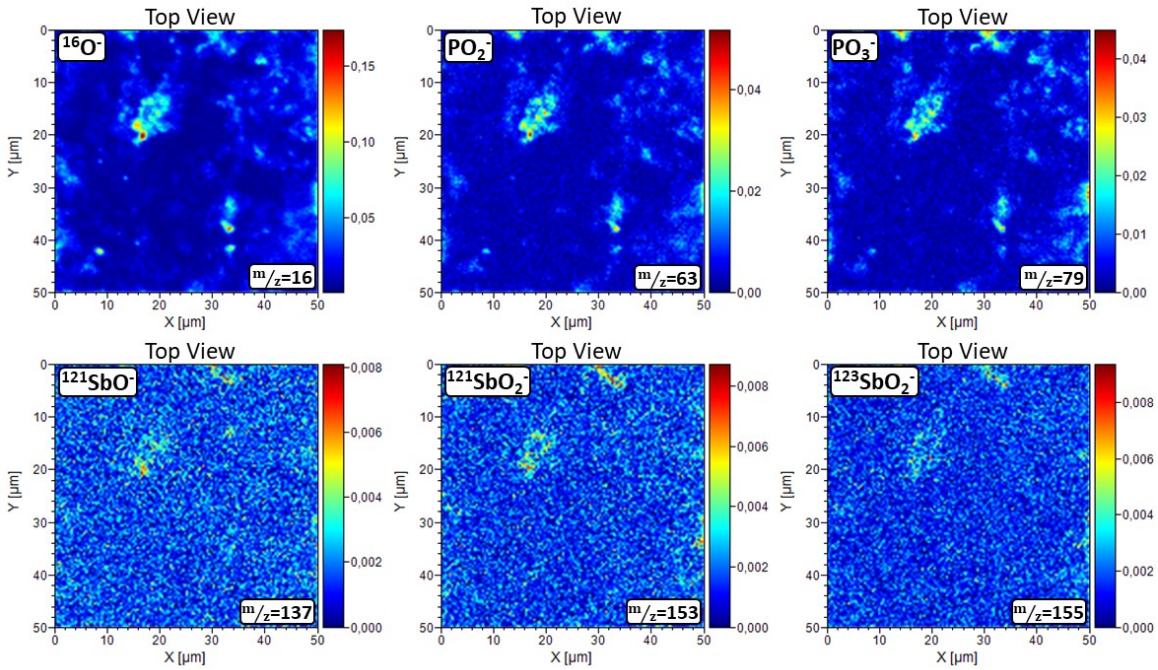

Figure S6. Lateral profiles of O and O-containing species in the field of view of the TOF-SIMS illustrate enhanced antimony oxide formation in O-rich areas. Possible O-source: PO_2^- / PO_3^-.

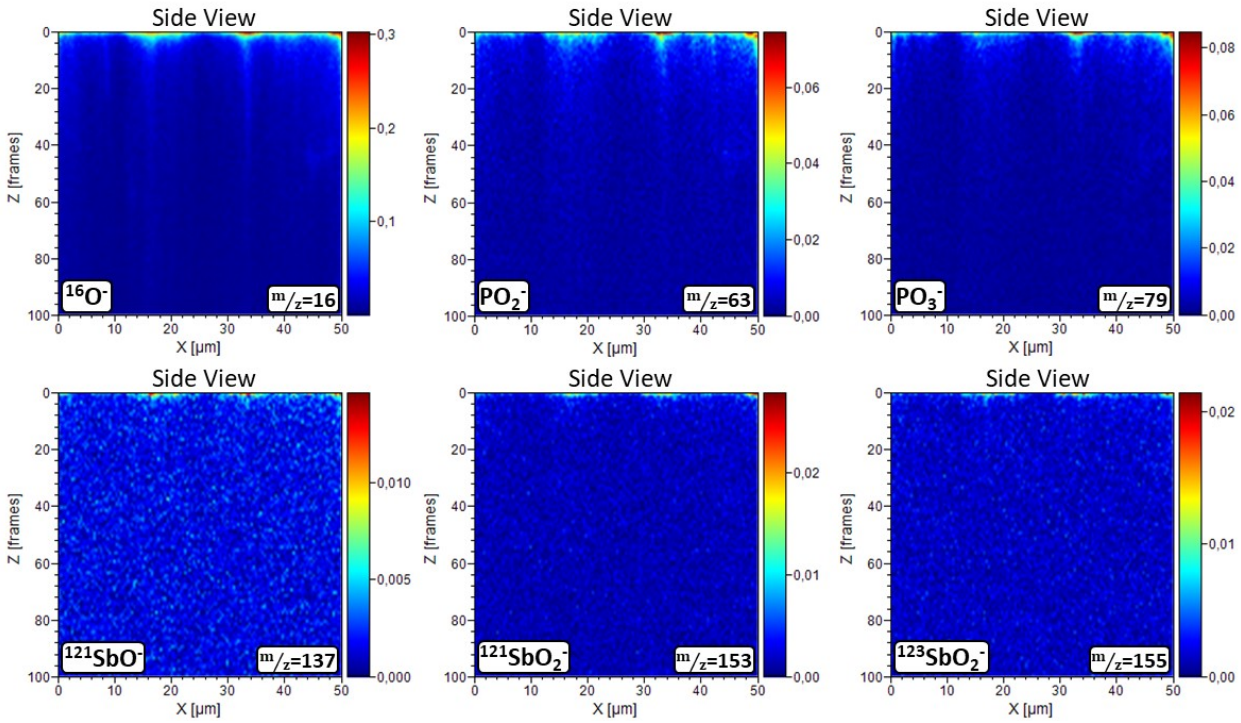

Figure S7. Side profiles of O and O-containing species in the field of view of the TOF-SIMS. The O-signals mainly arises from surface species on the agglomerates.

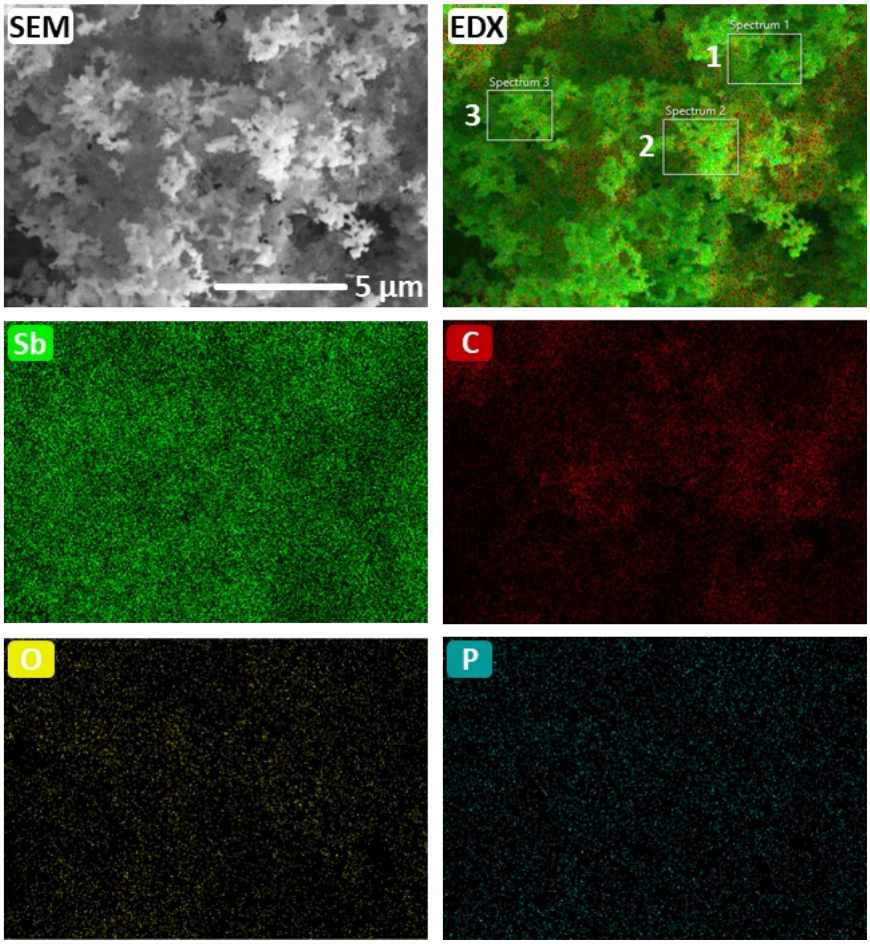

Figure S8. EDX mapping on an agglomerate of the Sb-C powder. The mappings illustrate the distribution of Sb (green), C (red), O (yellow), P (turquoise).

Table S3. Weight proportions of elements in Sb-C powder based on EDX analysis. Pre-synthesis ratio: Sb:C – 88.9 : 11.1 wt.%.

	Total section		Spectrum 1		Spectrum 2		Spectrum 3	
	Total / wt.%	Sb:C / wt.%	Total / wt.%	Sb:C / wt.%	Total / wt.%	Sb:C / wt.%	Total / wt.%	Sb:C / wt.%
Sb	83.11	**84.3**	88.8	**89.8**	84.53	**85.6**	90.32	**91.3**
C	15.54	**15.7**	10.12	**10.2**	14.27	**14.4**	8.61	**8.7**
O	1.15	-	0.89	-	1.06	-	0.98	-
P	0.20	-	0.18	-	0.15	-	0.09	-

Statistical error for Sb & C < 0.18 wt.%; O & P < 0.05 wt.%

Table S4. Mole proportions of elements in Sb–C powder based on EDX analysis.

	Total section / mol.%	Spectrum 1 / mol.%	Spectrum 2 / mol.%	Spectrum 3 / mol.%
Sb	33.21	44.65	35.55	48.71
C	62.97	51.57	60.82	47.09
O	**3.5**	**3.42**	**3.39**	**4.01**
P	0.31	0.36	0.24	0.19

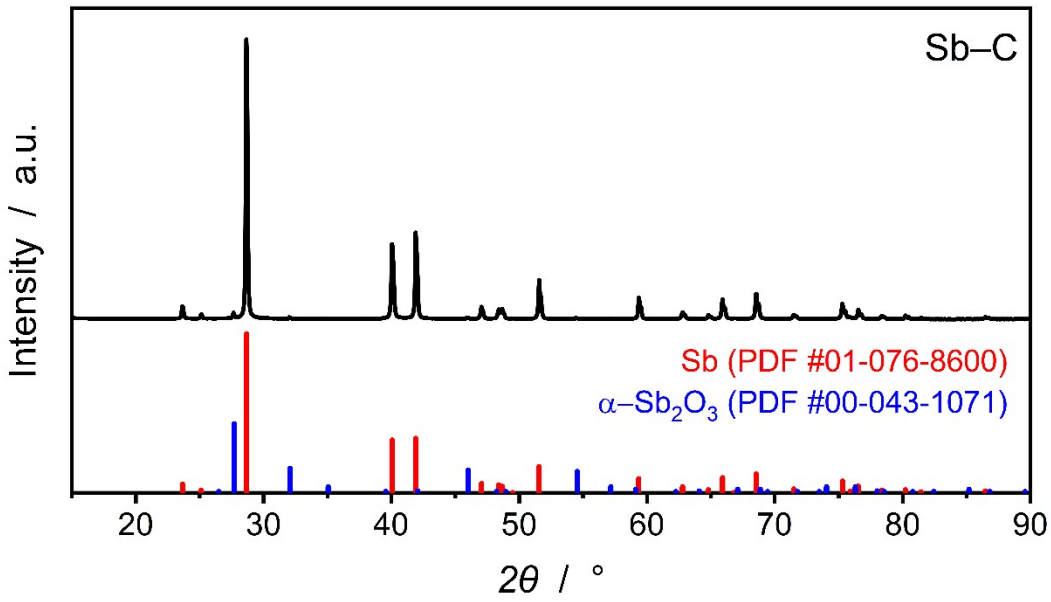

Figure S9. PXRD of microwave-assisted synthesized Sb–C powder using reduction agent $NaH_2PO_2 \cdot H_2O$ (top) and the expected reflection positions of antimony in rhombohedral crystal structure (space group $R\bar{3}m$) and senarmontite (α-Sb_2O_3) in cubic crystal structure (space group $Fd\bar{3}m$).

Table S5. Supplementary information to Figure 6 & Figure S10: Specific capacities and efficiencies of the cyclic voltammetry of the Sb/C composite anodes in Li- and Na system. Specific capacities and coulombic efficiencies (CE) were calculated based on the combined mass of the MW-synthesized powder and the added conductive carbon.

a)	Lithium / PVDF binder		
Cycle	Reduction / mAh $g_{Sb/C}^{-1}$	Oxidation / mAh $g_{Sb/C}^{-1}$	CE / %
1	690	297	43
2	99	60	61

b)	Lithium / PAA binder		
Cycle	Reduction / mAh $g_{Sb/C}^{-1}$	Oxidation / mAh $g_{Sb/C}^{-1}$	CE / %
1	733	614	84
2	632	561	89
3	594	558	94
4	595	554	93
5	600	550	92
13	575	535	93
25	537	480	89
30	394	348	88
35	176	150	85
40	119	98	82

c)	Sodium / PVDF binder		
Cycle	Reduction / mAh $g_{Sb/C}^{-1}$	Oxidation / mAh $g_{Sb/C}^{-1}$	CE / %
1	763	349	46
2	223	114	51

d)	Sodium / PAA binder		
Cycle	Reduction / mAh $g_{Sb/C}^{-1}$	Oxidation / mAh $g_{Sb/C}^{-1}$	CE / %
1	741	522	70
2	571	531	93
3	543	523	96
4	539	521	97
5	536	520	97
13	525	517	98
25	526	515	98
30	526	515	98
35	524	519	99
40	527	515	98

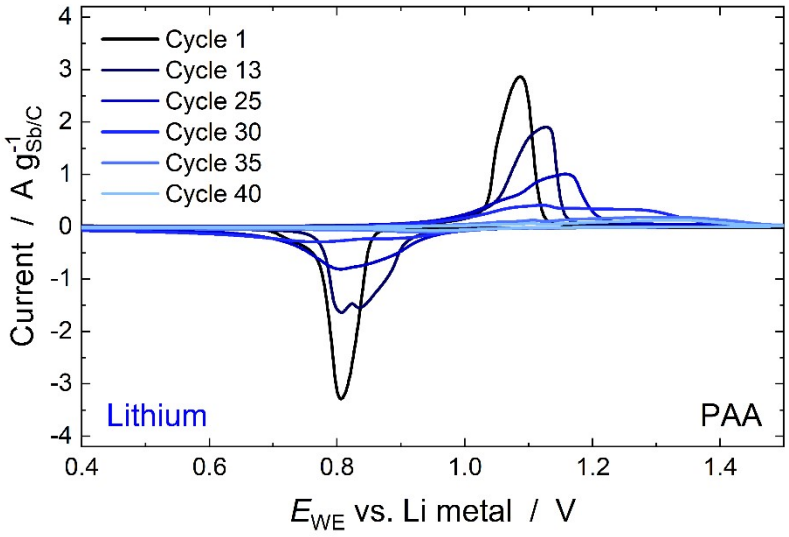

Figure S10. Cyclic Voltammetry on Sb/C composite anodes in Li-system. Specific currents were calculated based on the combined mass of the MW-synthesized powder and the added conductive carbon.

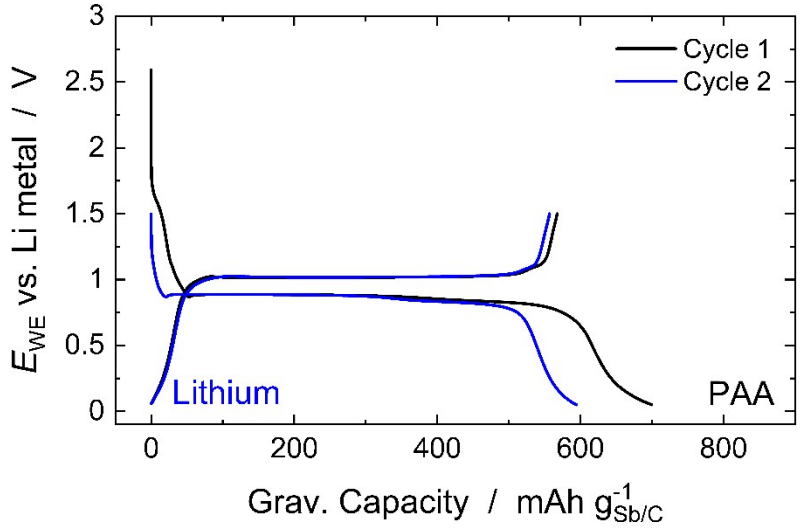

Figure S11. Galvanostatic cycling with potential limitation at 0.2 C (1 C = 660 mA g_{Sb}^{-1}) on Sb/C composite anodes: profiles of first two cycles in Li half-cell. Specific capacities were calculated based on the combined mass of the MW-synthesized powder and the added conductive carbon.

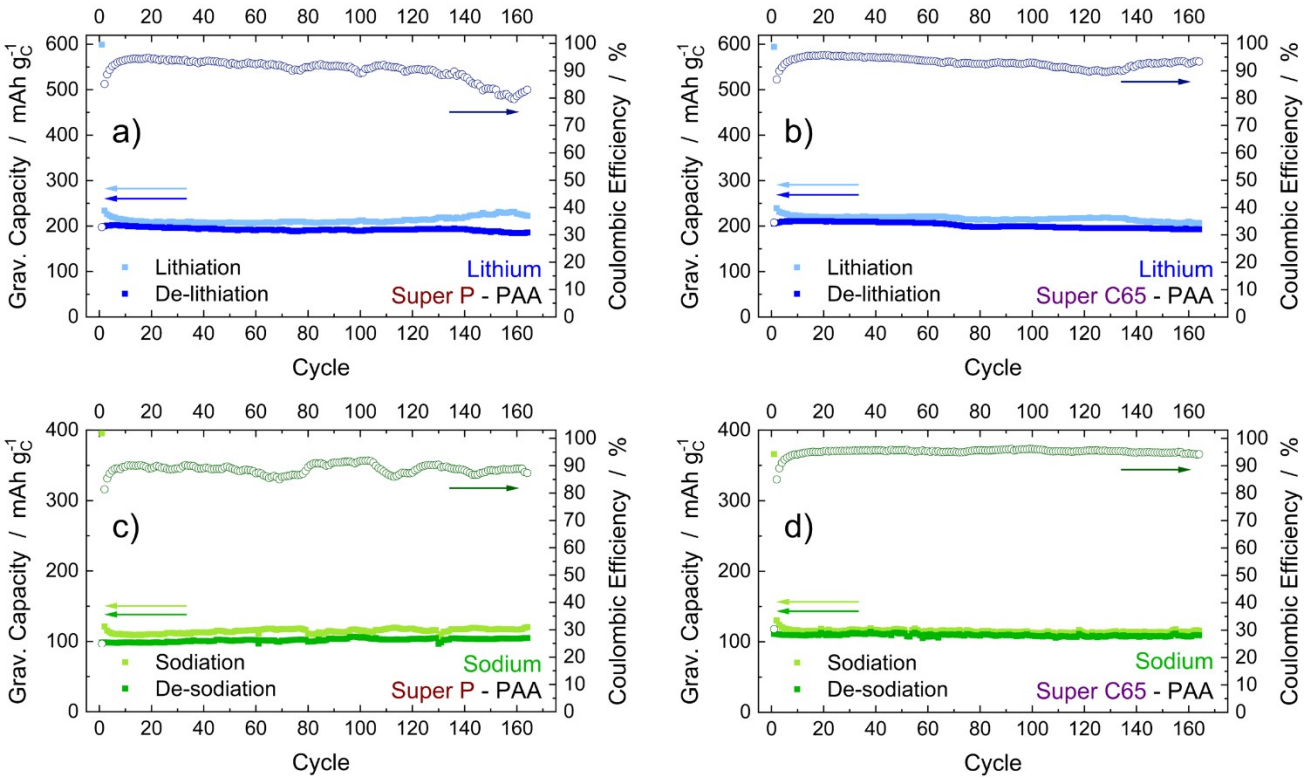

Figure S12. Galvanostatic cycling at 100 mA g_C^{-1}: **a)** Super P and **b)** Super C65 in Li-half cell; **c)** Super P and **d)** Super C65 in Na-half cell.

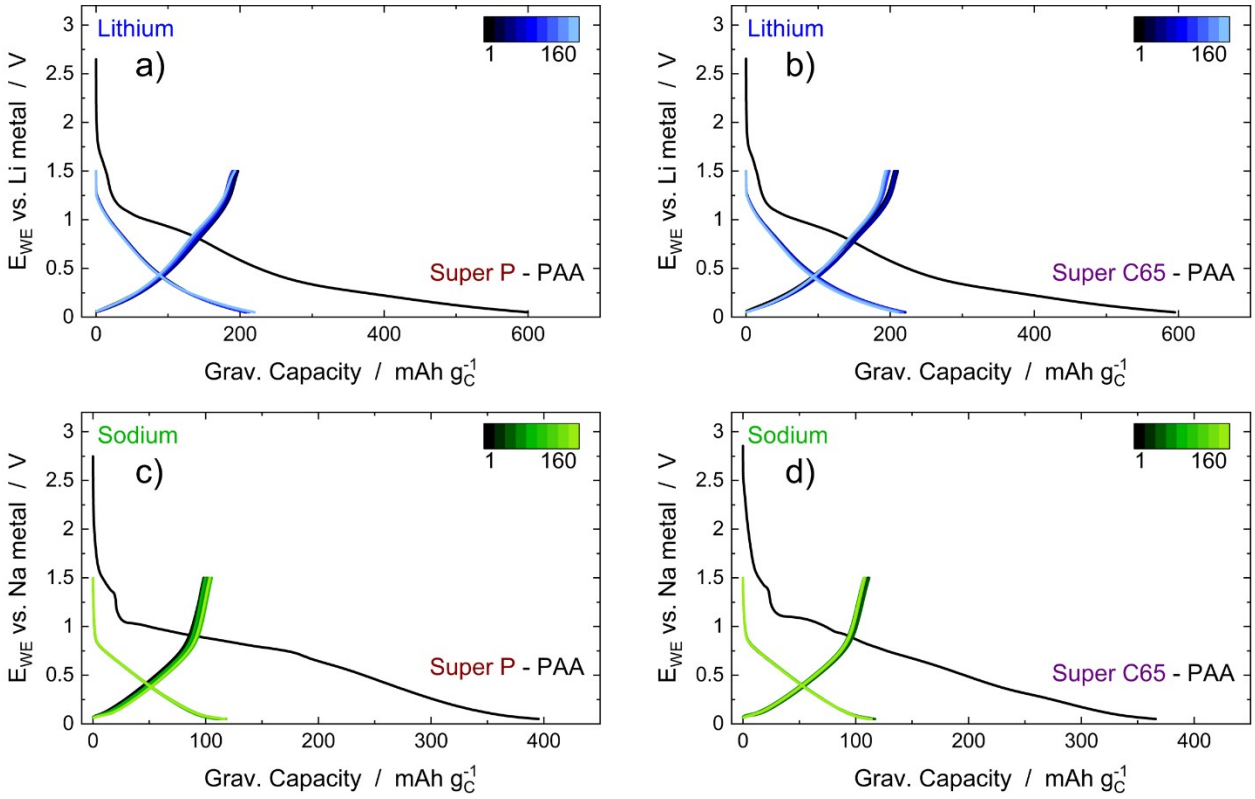

Figure S13. Galvanostatic profile at 100 mA g_C^{-1}. **a)** Super P and **b)** Super C65 in Li-half cell; **c)** Super P and **d)** Super C65 in Na-half cell.

Equation S1. Formula for calculating the intrinsic cycle-specific capacity of Sb, obtained by subtracting the capacity contributions of Super P and Super C65 from the total measured capacity. To accurately isolate the active contribution of Sb, the capacities of the conductive carbon additives were subtracted individually for each half-cycle (e.g., the discharge capacity in cycle 50 of the Sb/C composite anode was corrected by subtracting the discharge capacities of Super P and Super C65 in cycle 50).

$$q_{Sb,i} = \frac{q_{Sb/C,i} \cdot m_{Sb/C} - (q_{SuperP,i} \cdot m_{SuperP} + q_{SuperC65,i} \cdot m_{SuperC65})}{m_{Sb}}$$

q_s … specific capacity // m_s … mass in anode // s … species // i … half-cycle (red or ox)

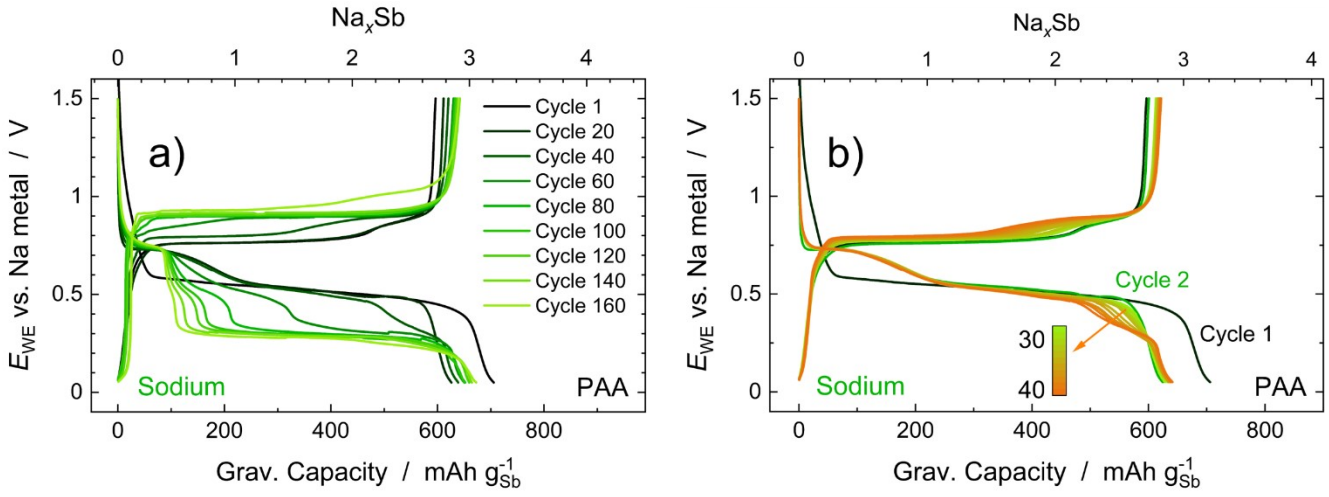

Figure S 14. Galvanostatic cycling at 0.2 C (1 C = 660 mA g_{Sb}^{-1}) on Sb/C composite anodes: sodiation profiles for a) cycles 1 to 160 b) cycles 1 to 40. Capacities are normalized exclusively to Sb, considering both mass and electrochemical contribution.

Equation S2. For key aspects see equation S1. The time dependence of the profile was taken into account by subtracting the carbon capacity proportionally to the state of reduction or oxidation. This approximation is justified, because Sb contributes ca. 96 % of the total capacity and a large portion of the hard carbon capacity has already reacted at E_{WE} (vs. Na metal) = 0.50 V, so the overall shape of the galvanostatic profile remains essentially unaffected. For Super P and Super C65 (Table S6) capacities, the arithmetic mean of either the reduction or oxidation capacities was used, except for the first reduction, where the first-cycle reduction capacities were used to account for surface contribution associated with side reactions.

$$q_{Sb,h}(t) = \frac{q_{Sb/C,h}(t) \cdot m_{Sb/C} - (q_{SuperP,\emptyset} \cdot m_{SuperP} + q_{SuperC65,\emptyset} \cdot m_{SuperC65}) \cdot \frac{q_{Sb/C,h}(t)}{q_{Sb/C,h,max}}}{m_{Sb}}$$

q_s … specific capacity // m_s … mass in anode // s … species // $\emptyset$ … mean capacity of hard carbons over 160 cycles (red or ox) // max … capacity at the end of half-cycle h // t … time

Table S6. 1st cycle reduction capacity and mean capacity during red/ox of hard carbon anodes (Figure S12).

	Capacity / mAh g_c^{-1}					
	1st cycle reduction		Mean during reduction		Mean during oxidation	
	Super P	Super C65	Super P	Super C65	Super P	Super C65
Na	395	366	115	115	102	109
Li	599	595	213	217	193	202

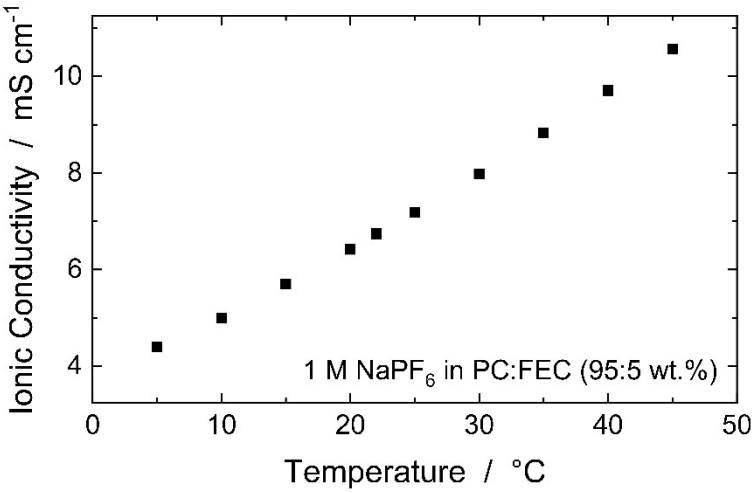

Figure S15. Ionic conductivity of the 1 M $NaPF_6$ in PC:FEC (95:5 wt.%) as a function of temperature between 5 °C and 45 °C. Conductivities were determined by electrochemical impedance spectroscopy using a temperature-controlled microcell setup.

Table S7. Temperature dependent ionic conductivity of 1 M $NaPF_6$ in PC:FEC (95:5 wt.%) and the corresponding electrolyte related ohmic drop ΔV_{el}. Values were calculated according to Equation S3 using the separator thickness of 0.052 cm and an applied current density of 0.223 mA cm^{-2}.

Temperature / °C	Ionic Conductivity / mS cm^{-1}	ΔV_{el} / mV
5	4.39	2.64
10	4.99	2.32
15	5.69	2.03
20	6.42	1.81
22	6.74	1.72
25	7.18	1.61
30	7.98	1.45
35	8.83	1.31
40	9.71	1.19
45	10.56	1.10

Equation S3. Correlation used to estimate the electrolyte related ohmic contribution to the cell voltage.

$$\Delta V_{el} = i\frac{L}{\kappa}$$

ΔV_{el} … ohmic drop across the electrolyte // i … current density // L … separator thickness // κ … ionic conductivity

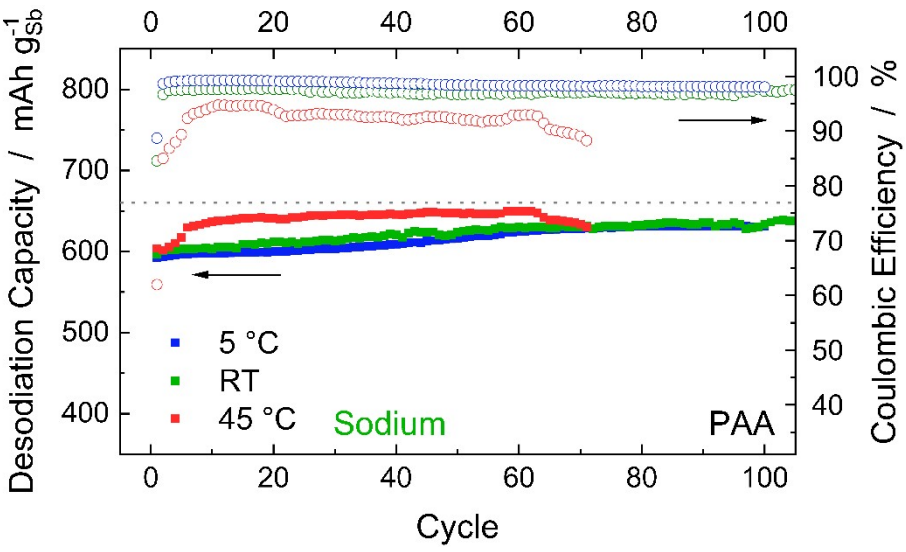

Figure S16. Galvanostatic cycling at 0.2 C (1 C = 660 mA g_{Sb}^{-1}) on Sb/C composite anodes: (dis)charge capacities and corresponding Coulombic efficiencies for 100 cycles at 5 °C, RT and 45 °C. The dashed line indicates 660 mAh g_{Sb}^{-1} – the theoretical limit. Capacities are normalized exclusively to Sb, considering both mass and electrochemical contribution – carbon capacities were approximated by utilizing the practical capacities of Super P and Super C65 obtained at room temperature (Table S6).

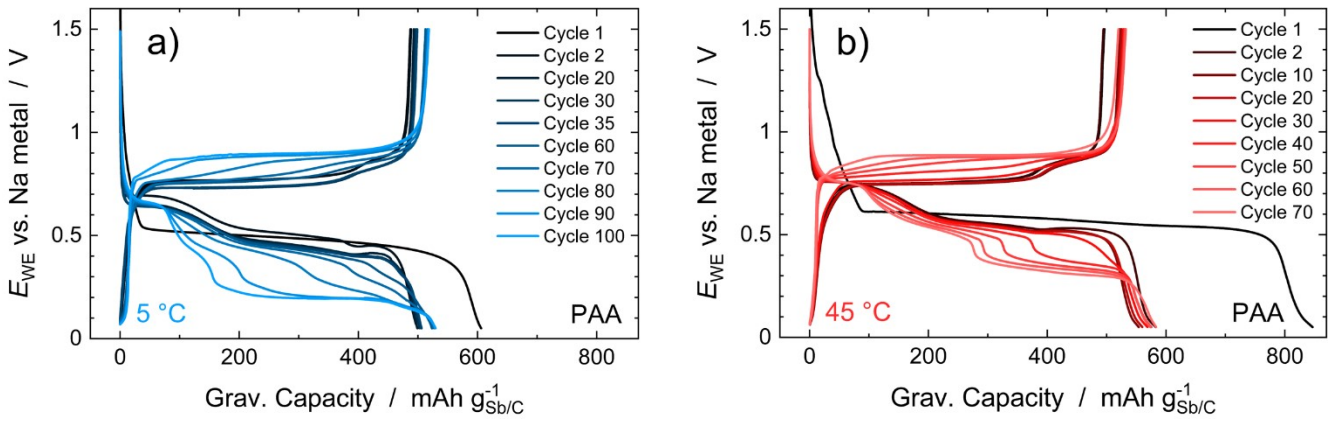

Figure S17. Galvanostatic profiles of Sb/C composite anodes cycled at 0.2 C (1 C = 660 mA g_{Sb}^{-1}) in Na half-cells at **a)** 5 °C and **b)** 45 °C. Specific capacities were calculated based on the combined mass of the MW-synthesized powder and the added conductive carbon.

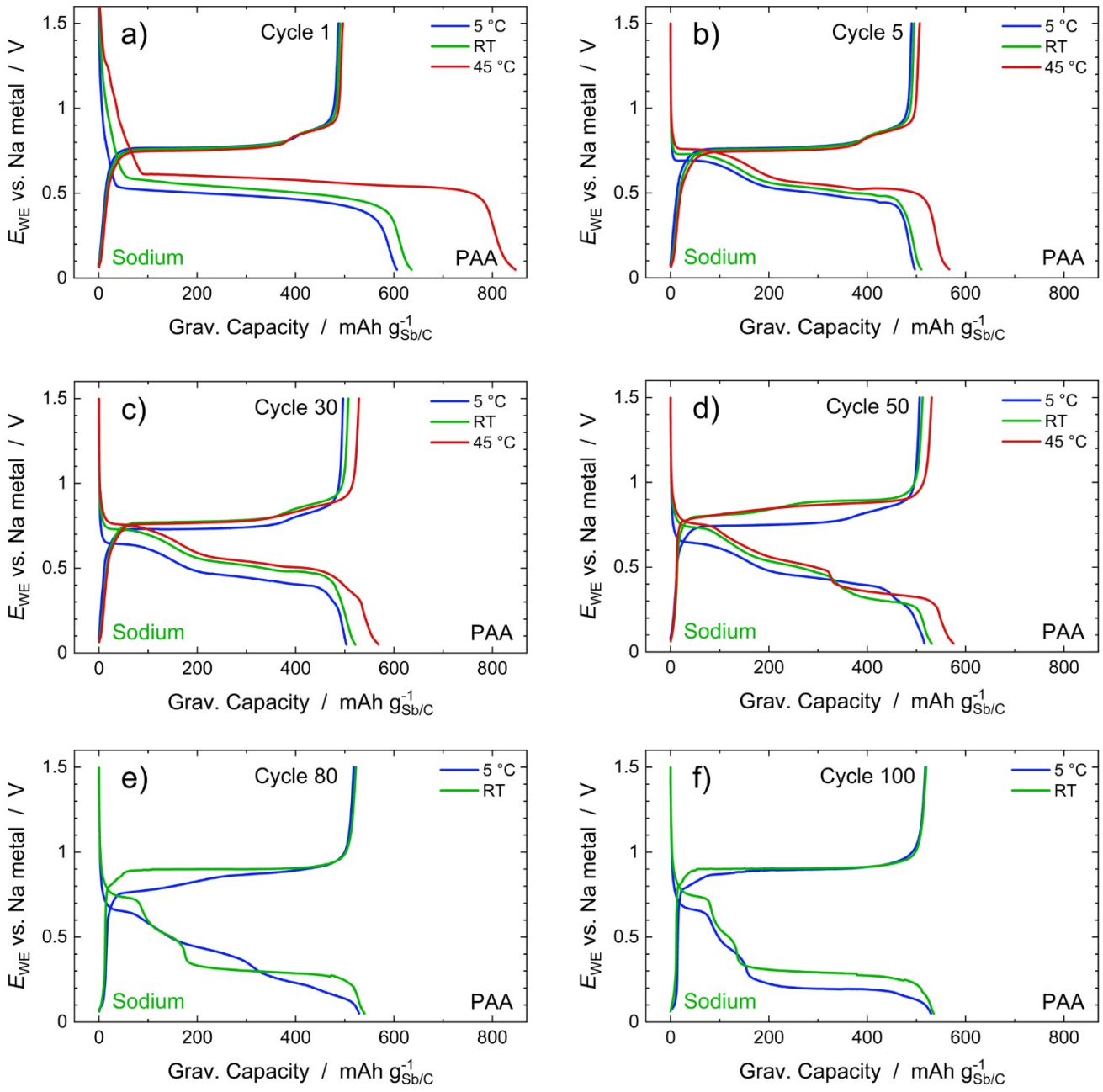

Figure S18. Comparison of galvanostatic profiles of Sb/C composite anodes cycled at 0.2 C (1 C = 660 mA g_{Sb}^{-1}) in Na half-cells at 5 °C, RT and 45 °C: **a)** cycle 1, **b)** cycle 5, **c)** cycle 30, **d)** cycle 50, **e)** cycle 80 and **f)** cycle 100. Specific capacities were calculated based on the combined mass of the MW-synthesized powder and the added conductive carbon.

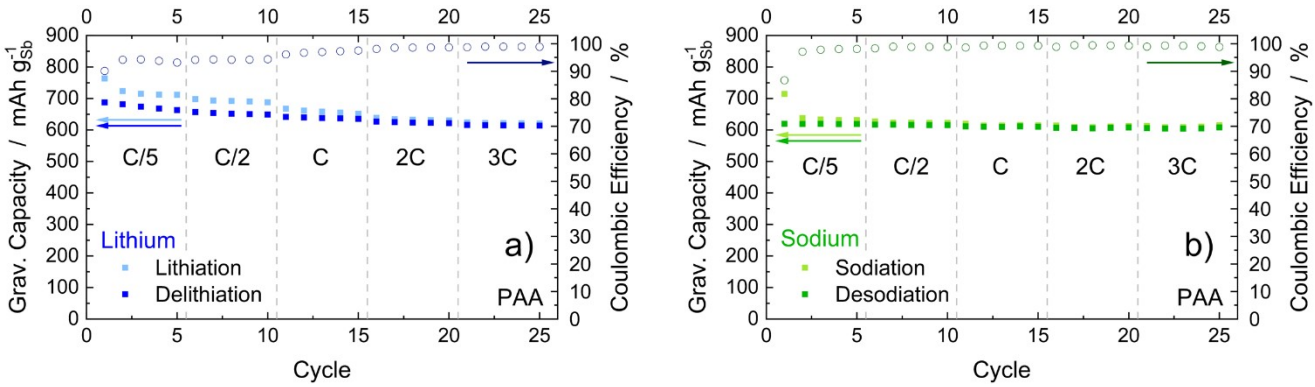

Figure S19. Galvanostatic cycling with potential limitation at C-rates between 0.2 C to 3 C (1 C = 660 mA g_{Sb}^{-1}) on Sb/C composite anodes: (dis)charge capacities and corresponding Coulombic efficiencies in **a)** Li half-cell and **b)** Na half-cell. Capacities are normalized exclusively to Sb, considering both mass and electrochemical contribution. Carbon capacities were approximated by utilizing the practical capacities of Super P and Super C65 obtained at room temperature (Table S6).

REFERENCES

(1) Chusuei, C. C.; Goodman, D. W.; van Stipdonk, M. J.; Justes, D. R.; Schweikert, E. A. Calcium Phosphate Phase Identification Using XPS and Time-of-Flight Cluster SIMS. *Analytical chemistry* **1999**, *71* (1), 149–153. DOI: 10.1021/ac9806963.

(2) Hirokawa, K.; Li, Z.; Tanaka, A. Role of electronegativity in the qualitative inference of the TOF-SIMS fragment pattern of inorganic compounds. *Fresenius' journal of analytical chemistry* **2001**, *370* (4), 348–357. DOI: 10.1007/s002160100811.

(3) Mokoena, P. P.; Gohain, M.; Kumar, V.; Bezuidenhoudt, B.; Swart, H. C.; Ntwaeaborwa, O. M. TOF SIMS analysis and enhanced UVB photoluminescence by energy transfer from Pr3+ to Gd3+ in Ca3(PO4)2:Gd3+,Pr3+ phosphor prepared by urea assisted combustion. *Journal of Alloys and Compounds* **2014**, *595*, 33–38. DOI: 10.1016/j.jallcom.2014.01.088.

(4) Kanyal, S. S.; Jensen, D. S.; Zhu, Z.; Linford, M. R. Multiwalled carbon nanotube forest grown via chemical vapor deposition from iron catalyst nanoparticles by ToF-SIMS. *Surface Science Spectra* **2015**, *22* (2), 29–33. DOI: 10.1116/1.4931984.

(5) Naraoka, H.; Aoki, D.; Fukushima, K.; Uesugi, M.; Ito, M.; Kitajima, F.; Mita, H.; Yabuta, H.; Takano, Y.; Yada, T.; Ishibashi, Y.; Karouji, Y.; Okada, T.; Abe, M. ToF-SIMS analysis of carbonaceous particles in the sample catcher of the Hayabusa spacecraft. *Earth Planet Sp* **2015**, *67* (1). DOI: 10.1186/s40623-015-0224-0.

(6) Baek, S.-D.; Biswas, P.; Kim, J.-W.; Kim, Y. C.; Lee, T. I.; Myoung, J.-M. Low-Temperature Facile Synthesis of Sb-Doped p-Type ZnO Nanodisks and Its Application in Homojunction Light-Emitting Diode. *ACS applied materials & interfaces* **2016**, *8* (20), 13018–13026. DOI: 10.1021/acsami.6b03258. Published Online: May. 16, 2016.

(7) Hein, A.; Martin, J.; Schäfer, M.; Weitzel, K.-M. Electrodiffusion versus Chemical Diffusion in Alkali Calcium Phosphate Glasses: Implication of Structural Changes. *J. Phys. Chem. C* **2017**, *121* (6), 3203–3211. DOI: 10.1021/acs.jpcc.6b11113.

(8) Kappen, P.; Ferrando-Miguel, G.; Reichman, S. M.; Innes, L.; Welter, E.; Pigram, P. J. Antimony leaching and chemical species analyses in an industrial solid waste: Surface and bulk speciation using ToF-SIMS and XANES. *Journal of hazardous materials* **2017**, *329*, 131–140. DOI: 10.1016/j.jhazmat.2017.01.022. Published Online: Jan. 15, 2017.

(9) Heiden, A. von der; Bornhöfft, M.; Mayer, J.; Martin, M. Oxygen diffusion in amorphous and partially crystalline gallium oxide. *Physical chemistry chemical physics : PCCP* **2019**, *21* (8), 4268–4275. DOI: 10.1039/C8CP06439C.

(10) Garrison, B.; Vickerman, J. C.; Briggs, D. *ToF-SIMS: Surface analysis by mass spectrometry*; Surface Spectra/IM Publications LLP, 2001.